Geophysical Journal International

Geophys. J. Int. (2012) **190,** 1761–1776 doi: 10.1111/j.1365-246X.2012.05592.x

Moment tensor inversion of waveforms: a two-step time-frequency approach

Václav Vavryčuk[1] and Daniela Kühn[2]

[1]*Institute of Geophysics, Academy of Sciences, Boční* II/1401*,* 141 00 *Praha* 4*, Czech Republic. E-mail: vv@ig.cas.cz*
[2]*NORSAR, Gunnar Randers vei* 15*, N-*2007 *Kjeller, Norway*

Accepted 2012 June 26. Received 2012 June 7; in original form 2011 December 21

SUMMARY

We present a moment tensor inversion of waveforms, which is more robust and yields more stable and more accurate results than standard approaches. The inversion is performed in two steps and combines inversions in time and frequency domains. First, the inversion for the source-time function is performed in the frequency domain using complex spectra. Second, the time-domain inversion for the moment tensor is performed using the source-time function calculated in the first step. In this way, we can consider a realistic, complex source-time function and still keep the final moment tensor inversion linear. Using numerical modelling, we compare the efficiency and accuracy of the proposed approach with standard waveform inversions. We study the sensitivity of the retrieved double-couple and non-double-couple components of the moment tensors to noise in the data, to inaccuracies of the location and of the velocity model, and to the type of the focal mechanism. Finally, the proposed moment tensor inversion is tested on real data observed in a complex 3-D inhomogeneous geological environment: a production blast and a rockburst in the Pyhäsalmi ore mine, Finland.

Key words: Earthquake dynamics; Earthquake source observations; Body waves; Computational seismology; Wave propagation; Dynamics and mechanics of faulting.

1 INTRODUCTION

The basic tool for quantifying earthquake sources is the seismic moment tensor. The moment tensor is calculated using amplitudes of seismic waves (Vavryčuk *et al.* 2008; Fojtíková *et al.* 2010; Godano *et al.* 2011), amplitude ratios (Miller *et al.* 1998; Hardebeck & Shearer 2003; Jechumtálová & Šílený 2005) or full waveforms (Dziewonski *et al.* 1981; Sipkin 1986; Kikuchi & Kanamori 1991; Šílený *et al.* 1992). The inversion of full waveforms is a widely used approach applicable on all scales: from micro- to large macro-earthquakes. It is usually applied employing the point-source approximation and assuming a time-independent focal mechanism. The inversion is performed in the time domain (Dreger & Woods 2002; Zahradník *et al.* 2005, 2008a,b; Sokos & Zahradník 2008; Adamová *et al.* 2009; Hingee *et al.* 2011) or in the frequency domain using amplitude spectra (Cesca *et al.* 2006) or complex spectra (Cesca & Dahm 2008; Vavryčuk 2011a,b). The inversion yields the moment tensor and, as a by-product, the common source-time function. The moment tensor is further decomposed into the double-couple (DC) and non-double-couple (non-DC) components (Miller *et al.* 1998; Vavryčuk 2001), which can be used to study the fault orientation, type of faulting (Vavryčuk *et al.* 2008; Vavryčuk 2011c) and physical properties of material in the source area (Vavryčuk 2004).

The waveform inversion is a data-demanding procedure: it needs an accurate source location, good knowledge of the velocity model and good azimuthal coverage of the focal sphere. The lack of data, an inaccurate location or an inaccurate velocity model produces errors and distorts the solution. The waveform inversion is a non-linear procedure that is usually performed in two steps. First, the waveforms are inverted for six moment-time functions using a linear inversion. Second, the moment-time functions are factorized into the moment tensor and the common source-time function using a non-linear approach. Because at least one part of the inversion is non-linear, it is essential to apply a robust inversion scheme and to perform a comprehensive analysis of accuracy to obtain reliable results (Šílený 1998; Jechumtálová & Šílený 2001; Wéber 2009).

To avoid difficulties with the non-linearity of the problem, the waveform inversion is often performed in the time domain under further simplifications. Because the primary goal usually is to retrieve the time-independent moment tensor but not the source-time function, the source-time function is identified with the step function (or the source-time rate function with the Dirac delta function, respectively) and the complexities in the source-time history are neglected. In this case, the inversion is linear and computationally undemanding (Zahradník *et al.* 2005, 2008a). The inversion, however, requires heavy filtering of high frequencies, which increases low-frequency noise in the data. If the heavy high-frequency filtering is not feasible, high frequencies can be kept in the signal to some extent, and the linear inversion is performed in iterations (Kikuchi & Kanamori 1991). Obviously, the accuracy of the successive iterations decreases rapidly, and the moment tensor as well as the source-time function are retrieved very approximately.

In this paper, we propose a new inversion scheme for computing time-independent moment tensors, which is more robust and yields more stable and more accurate results than the standard approaches. We follow the idea of Cesca *et al.* (2010) and Vallée *et al.* (2011) and adopt a multistep strategy to increase the efficiency of the inversion. The proposed inversion is performed in two steps and combines inversions in the time and frequency domains. First, the inversion for the source-time function is performed in the frequency domain using complex spectra. Second, the time-domain inversion for the moment tensor is performed using the source-time function calculated in the first step. In this way, we consider a more realistic (and potentially complex) source-time function and still keep the final moment tensor inversion linear. By numerical modelling, we compare the efficiency and accuracy of our approach with the standard waveform inversions. We study its sensitivity to noise in the data, to inaccuracies of the location and of the velocity model, and to the type of focal mechanism. Finally, the proposed moment tensor inversion is tested on real data observed in a complex 3-D inhomogeneous geological environment: a production blast and a rockburst in the Pyhäsalmi ore mine, Finland.

2 METHOD

2.1 Frequency-domain waveform inversion for moment-time functions

In the time domain, the representation theorem for a seismic point source reads (Aki & Richards 2002, eq. 3.23)

$$u_i(\mathbf{x}, t) = M_{nk}(t) * G_{in,k}(\mathbf{x}, t), \tag{1}$$

where $\mathbf{u}(\mathbf{x}, t)$ is the displacement, $M_{nk}(t)$ is the time-dependent seismic moment tensor and $G_{in,k}(\mathbf{x}, t)$ is the spatial derivative of the Green's function. In the frequency domain, it transforms to

$$u_i(\mathbf{x}, \omega) = M_{nk}(\omega)\, G_{in,k}(\mathbf{x}, \omega). \tag{2}$$

Reducing the pairs of indices in $G_{kl,m}$

$$G_{k1} = G_{k1,1},\; G_{k2} = G_{k2,2},\; G_{k3} = G_{k3,3}.$$
$$G_{k4} = G_{k2,3} + G_{k3,2},\; G_{k5} = G_{k1,3} + G_{k3,1},$$
$$G_{k6} = G_{k1,2} + G_{k2,1}, \tag{3}$$

eq. (2) can be expressed in matrix notation

$$\mathbf{Gm} = \mathbf{d}. \tag{4}$$

$\mathbf{G}$ is the matrix of the Green's function derivatives, $\mathbf{m}$ is the vector containing the six moment components and $\mathbf{d}$ is the vector of displacements observed at stations 1 to N:

$$\mathbf{G} = \begin{bmatrix} G_{11}^{(1)} & G_{12}^{(1)} & G_{13}^{(1)} & G_{14}^{(1)} & G_{15}^{(1)} & G_{16}^{(1)} \\ G_{21}^{(1)} & G_{22}^{(1)} & G_{23}^{(1)} & G_{24}^{(1)} & G_{25}^{(1)} & G_{26}^{(1)} \\ G_{31}^{(1)} & G_{32}^{(1)} & G_{33}^{(1)} & G_{34}^{(1)} & G_{35}^{(1)} & G_{36}^{(1)} \\ \cdots & \cdots & \cdots & \cdots & \cdots & \cdots \\ G_{11}^{(N)} & G_{12}^{(N)} & G_{13}^{(N)} & G_{14}^{(N)} & G_{15}^{(N)} & G_{16}^{(N)} \\ G_{21}^{(N)} & G_{22}^{(N)} & G_{23}^{(N)} & G_{24}^{(N)} & G_{25}^{(N)} & G_{26}^{(N)} \\ G_{31}^{(N)} & G_{32}^{(N)} & G_{33}^{(N)} & G_{34}^{(N)} & G_{35}^{(N)} & G_{36}^{(N)} \end{bmatrix}, \tag{5}$$

$$\mathbf{m} = \left[M_{11}, M_{22}, M_{33}, M_{23}, M_{13}, M_{12}\right]^T, \tag{6}$$

$$\mathbf{d} = \left[u_1^{(1)}, u_2^{(1)}, u_3^{(1)}, u_1^{(2)}, u_2^{(2)}, u_3^{(2)}, \ldots, u_1^{(N)}, u_2^{(N)}, u_3^{(N)}\right]^T, \tag{7}$$

where the superscript identifies the station. Matrix $\mathbf{G}$ and vectors $\mathbf{m}$ and $\mathbf{d}$ are functions of frequency. The vector $\mathbf{m}$ of moment-time functions is obtained using the generalized inversion (Menke 1989)

$$\mathbf{m} = \mathbf{G}^{-g}\mathbf{d}, \tag{8}$$

$$\mathbf{G}^{-g} = \left[\mathbf{G}^T\mathbf{G}\right]^{-1}\mathbf{G}^T, \tag{9}$$

where $\mathbf{G}^{-g}$ is the generalized inverse of $\mathbf{G}$. Eq. (8) is solved for each frequency.

2.2 Source-time function

The moment-time functions $M_{nk}(\omega)$ calculated using eqs (8) and (9) can be transformed into $M_{nk}(t)$ by applying the inverse Fourier transform and factorized as follows:

$$M_{nk}(t) = M_{nk}S(t), \tag{10}$$

where M_{nk} is the seismic moment tensor, and $S(t)$ is the source-time function. The factorization physically means that the focal mechanism is independent of time. This is a simplification, which is not generally valid. In principle, the focal mechanisms can vary in time, for example if a fault has a complex geometry. Focal mechanisms can also depend on the frequency range of the studied waves, particularly, because of small-scale inhomogeneities and irregularities along the fault radiating high-frequency waves (Vavryčuk 2011b). However, the assumption of the time-independent focal mechanism is a good approximation to study an overall mechanism in the low-frequency range.

Factorization is a non-linear procedure, which may be intricate, if the moment-time functions differ from each other. The factorization is usually performed under the constraint that the source-time rate function is always positive. The inversion is then performed by applying robust non-linear solvers, for example, the genetic (Šílený 1998) or the simplex algorithms (Jechumtálová & Šílený 2001), or the inversion is linearized and solved iteratively (Wéber 2009). Another option is to apply the principal component decomposition (Jolliffe 1986) to the set of the moment-time functions and to identify the source-time function with the most dominant principal component (Vasco 1989). The other, less dominant components are assumed to reflect noise in the data, numerical errors of the inversion or to be related to minor mechanisms present in the source process.

In this paper, we apply no constraints to the source-time rate function in the inversion. The constraint to a non-negative source-time rate function is restrictive and not feasible for data filtered in a narrow frequency band. In addition, it is not applicable if velocity or acceleration records are inverted instead of displacements to suppress noise. The source-time rate function is sought using the principal component analysis (Vasco 1989).

The factorization yields both the source-time function and the moment tensor. If the moment-time functions have identical forms in time, the moment tensor components are obtained immediately as the scale factors between the moment-time functions and the source-time function. If the moment-time functions differ from each other in time, the factorization is more involved and may produce an unstable moment tensor. Therefore, it is preferable to improve the accuracy of the moment tensor further using a more robust procedure, for example, by applying another inversion performed in time domain as demonstrated in the next section. In this inversion, the inverted matrix will not be composed of the spatial derivatives of Green's functions, but of the spatial derivatives of elementary seismograms.

2.3 Time-domain inversion using elementary seismograms

The elementary seismograms and their spatial derivatives are defined as follows:

$$S_{in}(\mathbf{x}, t) = S(t) * G_{in}(\mathbf{x}, t), \tag{11}$$

$$S_{in,k}(\mathbf{x}, t) = S(t) * G_{in,k}(\mathbf{x}, t), \tag{12}$$

being the time convolution of the Green's functions and the source-time function. The representation theorem (1) can be amended to read

$$u_i(\mathbf{x}, t) = M_{nk} S_{in,k}(\mathbf{x}, t). \tag{13}$$

In contrast to eq. (1), this equation contains no time convolution and can be solved readily. The seismic moment tensor is inverted in the time domain using the generalized inversion

$$\mathbf{m} = \mathbf{S}^{-g}\mathbf{d}, \tag{14}$$

where $\mathbf{m}$ is no longer a function of frequency or time. In contrast to eq. (8) which is solved for each frequency separately, eq. (14) is solved just once using the least squares method and involves amplitudes at all stations and at all times. The inversion combines the following two advantages: it takes into account the complex source-time history and yet it is linear.

3 NUMERICAL MODELLING

In this section, the efficiency of the proposed inversion is tested numerically and compared with other standard methods. Their stability and robustness is analysed using repeated inversions of synthetic data contaminated by random noise. We apply two kinds of noise: first, the waveforms are distorted by superimposing noise in amplitudes, and second, the waveforms are slightly shifted in time. Distorting amplitudes of the waveforms simulates the errors in waveform modelling because of an inaccurate velocity model including attenuation as well as influence of seismic noise, which is always present in observations. Shifting of waveforms in time simulates effects produced by inaccurate locations and an inaccurate velocity model.

The stability of the moment tensor inversion is often estimated in case studies using the jack-knife test, when the inversion is performed repeatedly for various configurations of subsets of seismic stations. Because our primary goal is not to assess the quality of the station configuration and its influence on the results, but the robustness of different inversion methods for the same station configuration, this test is omitted here.

3.1 Configuration of the experiment

The configuration of stations, the velocity model and the source location mimic observations at the Pyhäsalmi ore mine, Finland (Oye *et al.* 2005). The seismic network consists of 12 vertical sensors and 4 three-component sensors. To compute synthetic data, we placed the source at the same position as the production blast analysed in Section 4 where real observations are analysed. The coverage of the focal sphere is almost uniform (see Fig. 1a). The source-receiver distances range from 60 to 400 m. The velocity model is strongly heterogeneous. It consists of rocks characterized by two different velocities as well as large areas of cavities (see Table 1). The Green's functions are computed using the 3-D finite difference viscoelastic code E3D (Larsen & Grieger 1998) on a 2-m spatial grid. The central frequency of the Gaussian source pulse is 350 Hz. The sampling rate is 10 kHz. The synthetic source-time rate function has duration of 30 ms and displays two distinct maxima (see Figs 1b and c). The focal mechanism is assumed to be alternatively a pure double-couple with strike, dip and rake of 45°, 45° and 90°, or purely explosive.

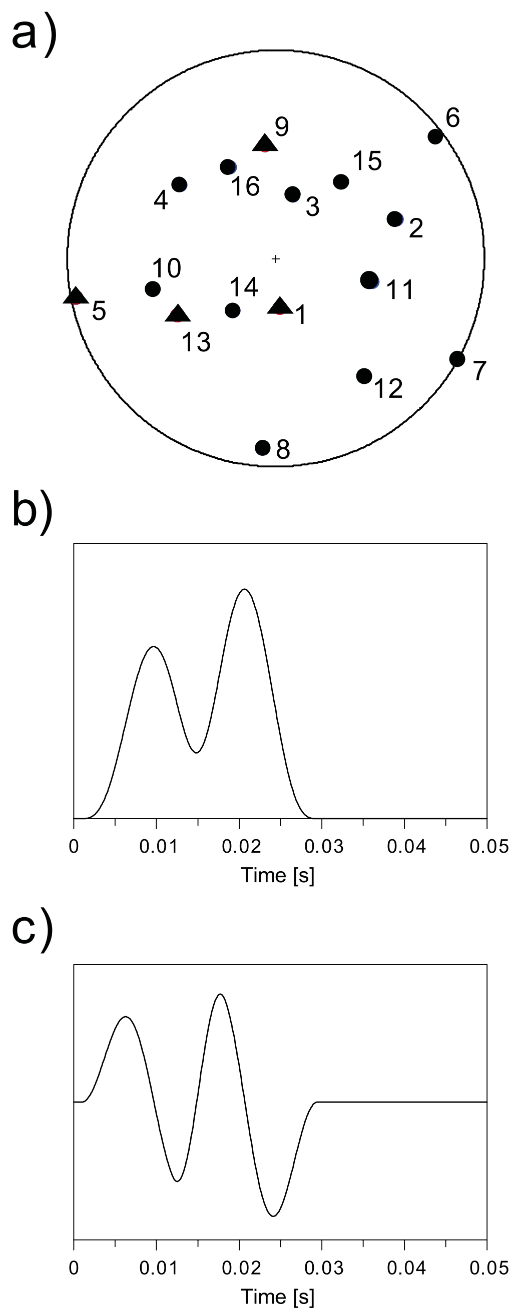

Figure 1. Focal sphere coverage (a), the first derivative of the source-time function (b) and the second derivative of the source-time function (c). Dots and triangles in plot (a) mark one-component and three-component sensors, respectively. The numbers in (a) identify the stations.

Table 1. Parameters of the velocity model.

	v_P (m s^{-1})	v_S (m s^{-1})	ρ (kg m^{-3})
Excavation area	300	0	1.25
Host rock	6000	3460	2000
Ore body	6300	3700	4400

3.2 Synthetic waveforms

Synthetic waveforms are calculated using eqs (1) and (10) from Green's functions $\mathbf{G}(\mathbf{x}, t)$, moment tensor $\mathbf{M}$ and source-time function $S(t)$. The waveforms are contaminated by random noise and are slightly shifted in time as discussed above. The statistical distribution of random noise in amplitudes and time shifts is uniform. The level of noise varies from 0 (noise-free data) to 100 per cent of the maximum amplitude of the noise-free signal (very noisy data) in steps of 5 per cent. The maximum random time shifts vary from 0 to 10 ms in steps of 0.5 ms. The data as well as the Green's functions are filtered by a two-sided Butterworth high-pass filter with a corner frequency of 20 Hz to remove low-frequency noise.

Figs 2(a) and (b) show synthetic noise-free waveforms and waveforms contaminated by noise with a noise level of 75 per cent. The waveforms are complex, characterized by long coda waves. The P waves are hardly notable in this frequency range. The seismic energy is mainly radiated in S waves.

3.3 Inversion methods

The accuracy and efficiency of the proposed inversion scheme is tested and compared with two other inversions called Inversion A and Inversion B.

Inversion A is the simplest inversion scheme used in this paper. It is a time-domain inversion where both waveforms and Green's functions are filtered to have an identical frequency content using a two-sided Butterworth low-pass filter with a corner frequency of 100 Hz. The actual time dependence of the source-time function is neglected being approximated by the Dirac delta function. In this case, the time convolution in eq. (1) is reduced to a multiplication, and the moment tensor is calculated in the time domain using a system of equations similar to eq. (4). The inversion is accomplished for the time-independent moment tensor $\mathbf{M}$, and the equations include amplitudes recorded at all stations and at all times. The inversion is performed repeatedly with varying origin times, and the optimum solution is the one showing the highest correlation between the waveforms and synthetics.

Inversion B is the standard waveform inversion performed in the frequency domain using complex spectra (see eq. 8). The Green's functions and the data are filtered by a two-sided Butterworth low-pass filter with corner frequencies of 250 Hz and 160 Hz, respectively. The inversion is performed up to 400 Hz. The inversion produces six frequency-dependent moment-time functions, which are transformed into the time domain. The source-time function and the resultant moment tensor are factorized using the principal component analysis (Jolliffe 1986).

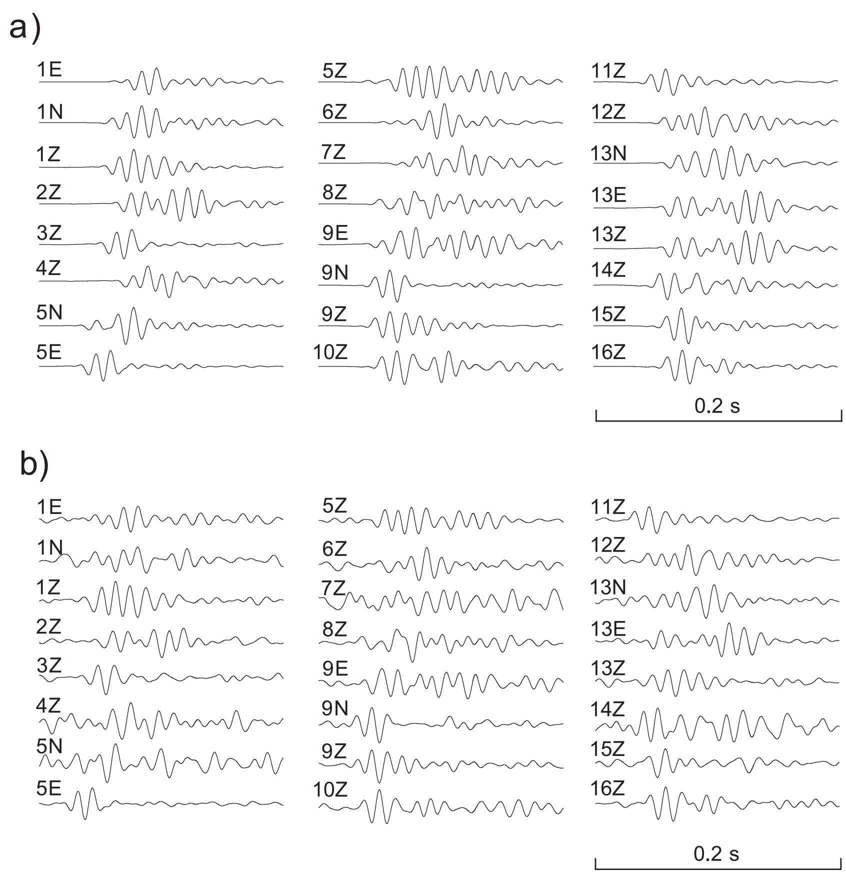

Figure 2. Synthetic noise-free (a) and noisy (b) waveforms for an explosive source. The maximum level of amplitude noise in plot (b) is 75 per cent. The waveforms are filtered by the two-sided Butterworth low-pass filter with a corner frequency of 100 Hz. A time interval of 0.2 s is shown. Each trace is identified by the station number and by the component.

Inversion C is the two-step time-frequency approach described in section 2 Method. The first step of the inversion is identical with Inversion B. The source-time function obtained using the principal component analysis is further convolved with the spatial derivatives of the Green's functions according to eq. (12) to obtain the elementary seismograms. Finally, the moment tensor is calculated using eq. (14).

In all inversions, the velocity records are inverted. The second time derivative of the source-time function is computed in Inversions B and C. This function can take positive as well as negative values, hence no constraint on the positivity of the function is applied in the factorization. All inversions are performed in two iterations. After the first iteration, the observed and synthetic waveforms at each sensor are cross-correlated to find their optimum alignment. The waveforms are shifted in time to yield the highest correlation with synthetics. The time shifts must lie within the range from -10 to 10 ms. This procedure suppresses errors in arrival times produced by an inaccurate event location or an inaccurate velocity model. In the second iteration, the inversion procedure is applied to the optimally aligned waveforms.

3.4 Results

The results of the inversion for the double-couple source are shown in Figs 3–5. The figures show the mean values (left-hand side plots) and the standard deviations (right-hand side plots) for the DC percentage (Fig. 3) and for the deviation of the P/T axes (Fig. 4). In addition, Fig. 5 shows the mean values for the isotropic (ISO) and the compensated linear vector dipole (CLVD) components. The mean values and the standard deviations are calculated from 100 realizations of random noise in amplitudes and random time shifts of records. Because all combinations of 20 levels in amplitude noise and 20 levels of time shift noise are computed, the figures summarize results of 40.000 inversions. The figures indicate that Inversions A and C are more sensitive to noise in the time shifts of the signal than to noise in amplitudes. For time shifts of less than 4–5 ms, both inversions work well. For larger time shifts, the DC percentage rapidly decreases and the P/T deviations rapidly increase. In addition, the standard deviations of the DC component and the P/T deviations become significant. The critical value of 4–5 ms corresponds to one-fourth of the cycle duration of the second derivative of the source-time function (see Fig. 1c).

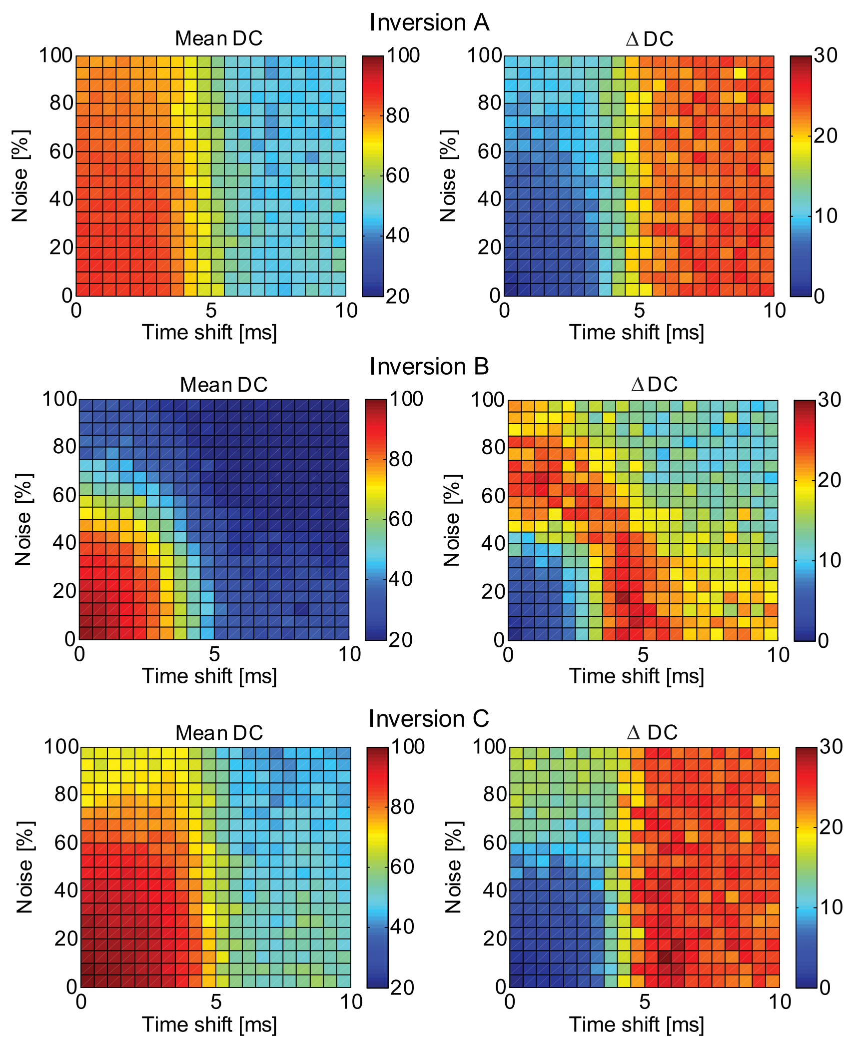

Figure 3. Inversion for the double-couple source: DC percentage. Mean values (left-hand side plots) and standard deviations (right-hand side plots) of the DC percentages are shown for Inversion A (upper plots), Inversion B (middle plots) and Inversion C (lower plots) as a function of noise in time shifts (x-axis) and in amplitudes (y-axis). The colour-coded mean values and the standard deviations are in per cent. The moment tensor decomposition into the DC and non-DC percentages is performed using the formulae of Vavryčuk (2001). The mean values and the standard deviations are calculated over 100 realizations of random noise.

Interestingly, Inversion B is significantly more sensitive to the noise in amplitudes than Inversions A and C. The inversion works well for noise up to 50 per cent. If the noise is higher, the accuracy of the inversion rapidly decreases. For high levels of amplitude noise and noise in time shifts, the DC percentage decreases from 100 per cent to only 20 per cent. At the same time, the ISO percentage increases from 0 per cent up to 65 per cent and the CLVD percentage from 0 per cent up to 20 per cent. The observation of extremely high spurious values of the ISO percentage is striking and evidently handicaps this type of inversion.

Comparing the efficiency of the three methods, the best results are obtained for Inversion C. Inversion A is stable and yields reasonable results even for high noise in amplitudes. However, this inversion is not accurate for low noise levels yielding biased results even for noise-free data in case of a complex source-time function (see Table 2). Inversion B is highly accurate provided the level of noise in amplitudes and in time shifts is low. Unfortunately, the accuracy rapidly decreases for higher levels of noise and the inversion tends to produce an enormously high spurious ISO percentage. Inversion C combines the advantages of both previous inversions. It yields unbiased results for noise-free data and high DC percentages, as well as low P/T deviations for the largest interval of noise in amplitudes and/or arrival times (see Table 2). The source-time function, the focal mechanisms and the fit between data and synthetics for the inversion of waveforms with an amplitude noise of 25 per cent and noise in arrival times of 5 ms are shown in Figs 6 and 7.

Similar conclusions as for the double-couple source can be drawn for the explosive source (see Fig. 8). Again, the best results are obtained for Inversion C. This method works well in the whole interval of amplitude noise and noise in arrival times. The worst results are obtained for Inversion A; Inversions B and C work significantly better (see Table 3). Interestingly, a critical value of noise in arrival times, beyond which the solution completely deteriorates, is missing in all three inversions. This means that the inversions are much more stable for the explosive source than for the double-couple source. Even for the highest values of noise in amplitudes and time shifts, the retrieved value of the ISO percentage is always higher than 75 per cent. For Inversion C, the ISO percentage even reaches values higher than 90 per cent. The source-time function, the focal mechanisms and the fit between the data and synthetics for the inversion of waveforms with an amplitude noise of 25 per cent and noise in arrival times of 5 ms are shown in Figs 9 and 10.

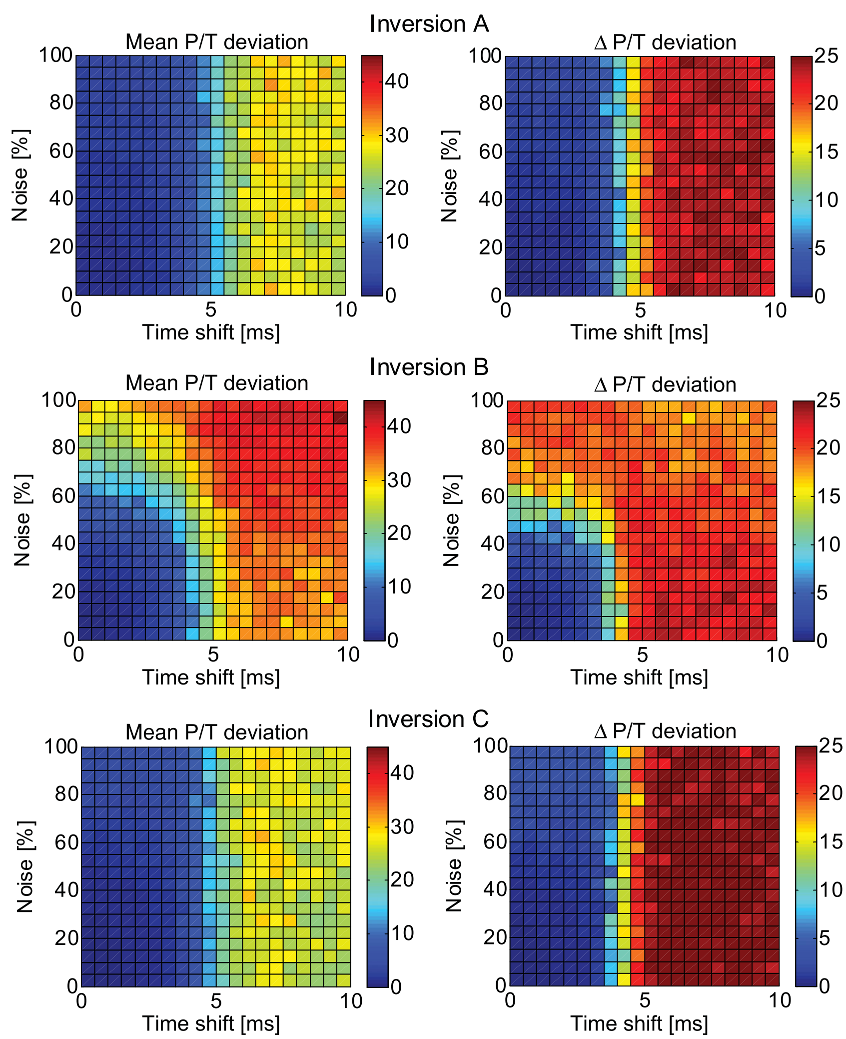

Figure 4. Inversion for the double-couple source: deviations of the P/T axes. Mean values (left-hand side plots) and standard deviations (right-hand side plots) of the deviations of the P/T axes are shown for Inversion A (upper plots), Inversion B (middle plots) and Inversion C (lower plots) as a function of noise in time shifts (*x*-axis) and in amplitudes (*y*-axis). The deviations of the P/T axes are defined as angles between the correct and retrieved P/T axes, respectively. The colour-coded mean values and standard deviations are in degrees.

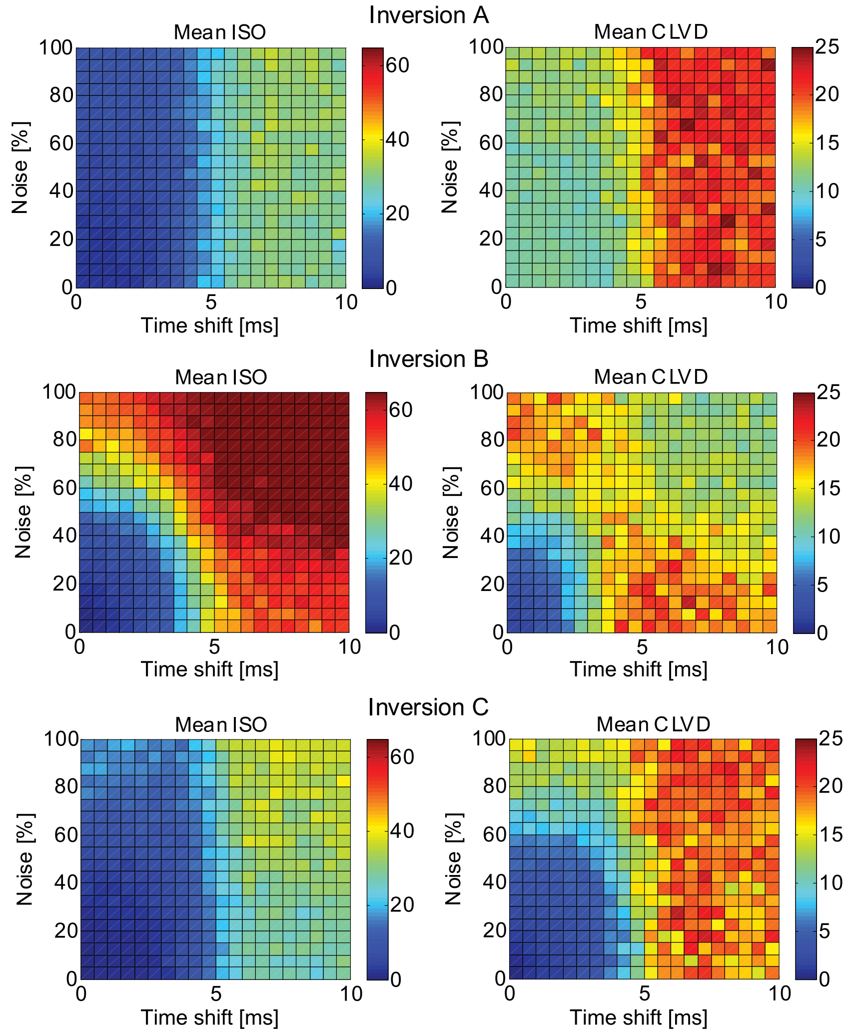

Figure 5. Inversion for the double-couple source: ISO and CLVD percentages. Mean absolute values of the ISO (left-hand side plots) and CLVD (right-hand side plots) percentages are shown for Inversion A (upper plots), Inversion B (middle plots) and Inversion C (lower plots) as a function of noise in time shifts (x-axis) and in amplitudes (y-axis). The colour-coded mean values of the ISO and CLVD components are in per cent.

Table 2. Inversion of the pure DC source.

	abs(ISO) (per cent)	abs(CLVD) (per cent)	DC (per cent)	δP (°)	δT (°)
True values	0.0	0.0	100.0	0.0	0.0
Noise-free data					
Inversion A	2.8	10.9	86.3	1.0	1.3
Inversion B	0.4	1.7	97.9	0.4	0.1
Inversion C	0.2	0.1	99.7	0.1	0.1
Noisy data					
Inversion A	17.9	14.6	67.5	10.9	11.0
Inversion B	57.9	13.4	28.7	28.0	26.6
Inversion C	18.0	13.4	68.6	11.7	15.9

Noisy data: the level of noise in amplitudes is 50 per cent, the level of noise in time shifts is 5 ms, mean values over 100 realizations of random noise are presented. Quantities abs(ISO) and abs(CLVD) are absolute values of ISO and CLVD, respectively, δP and δT are mean deviations between true and retrieved directions of the P and T axes, respectively. The ISO, CLVD and DC percentages are defined and calculated according to Vavryčuk (2001).

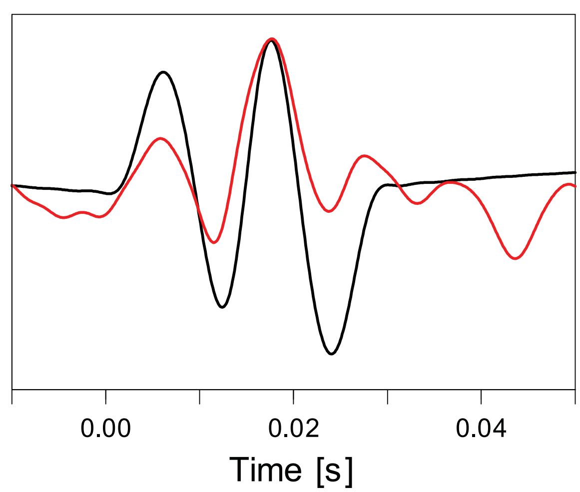

Figure 6. Second derivative of the source-time function retrieved from noise-free (black) and noisy (red) waveforms of the double-couple source. The inverted noisy waveforms are contaminated with noise in amplitudes up to 25 per cent and with noise in arrival times up to 5 ms.

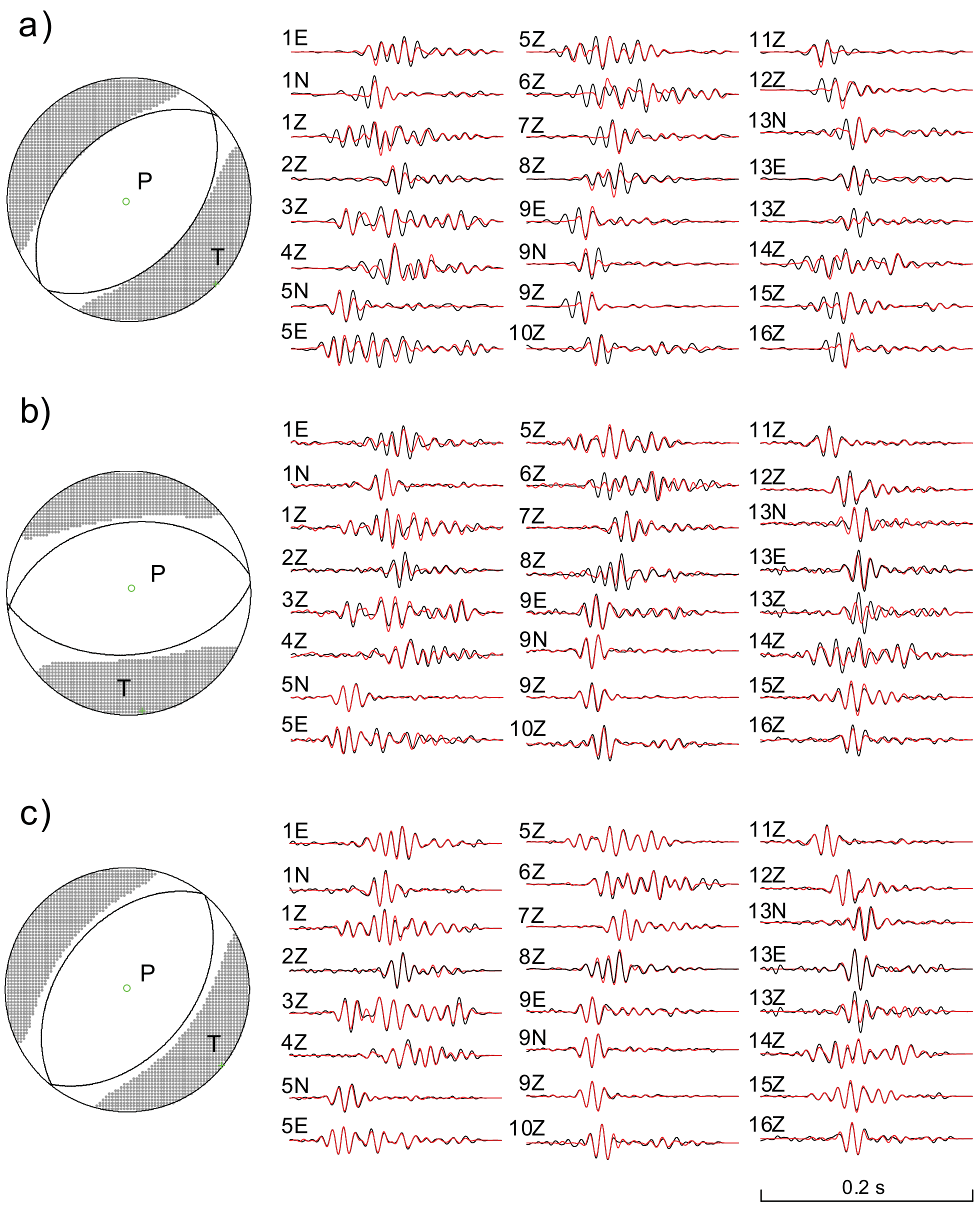

Figure 7. Inversion for the double-couple source: the focal mechanisms and the fit between the synthetic and observed data for Inversion A (upper plots), Inversion B (middle plots) and Inversion C (lower plots). Red lines—synthetic waveforms, black lines—observed data. The inverted waveforms are contaminated with noise in amplitudes up to 25 per cent and with noise in arrival times up to 5 ms.

4 APPLICATION TO OBSERVATIONS IN THE PYHÄSALMI ORE MINE, FINLAND

The moment tensor inversion is illustrated on observations of a production blast and a rockburst in the Pyhäsalmi ore mine, Finland.

4.1 Pyhäsalmi ore mine

The Pyhäsalmi ore mine in Finland (operated by INMET Mining Co.) extends to a depth of 1.4 km and is one of the deepest of its kind in Europe. Massive sulfide ores are located in the hinge of a large synform surrounded by felsic volcanics (Puustjärvi 1999). The ore forms a potato-shaped body (see Fig. 11a); its outer rim pyrite contains some zinc, the inner rim pyrite contains some copper, and the innermost part of the ore body consists of uneconomical pyrite.

The microseismic monitoring network was installed by the ISS International Ltd (Stellenbosch, South Africa). Sixteen 4.5 Hz geophones, four of which are three-component sensors, are cemented in boreholes drilled vertically in tunnel roofs and have been recording since January 2003 (Fig. 11b). The maximum sampling rate is 3 kHz, but records may be downsampled depending on the predominant frequency of the events.

Microseismic activity is strongest throughout the tunnel system and in stopes after excavation. The most seismically active regions correspond to the most active mining area. Approximately 1500 events per months are detected, two-third of which are production blasts. Typical source-receiver distances are 60–400 m. At short distances, *P*- and *S*-wave signals are short and impulsive, at distances

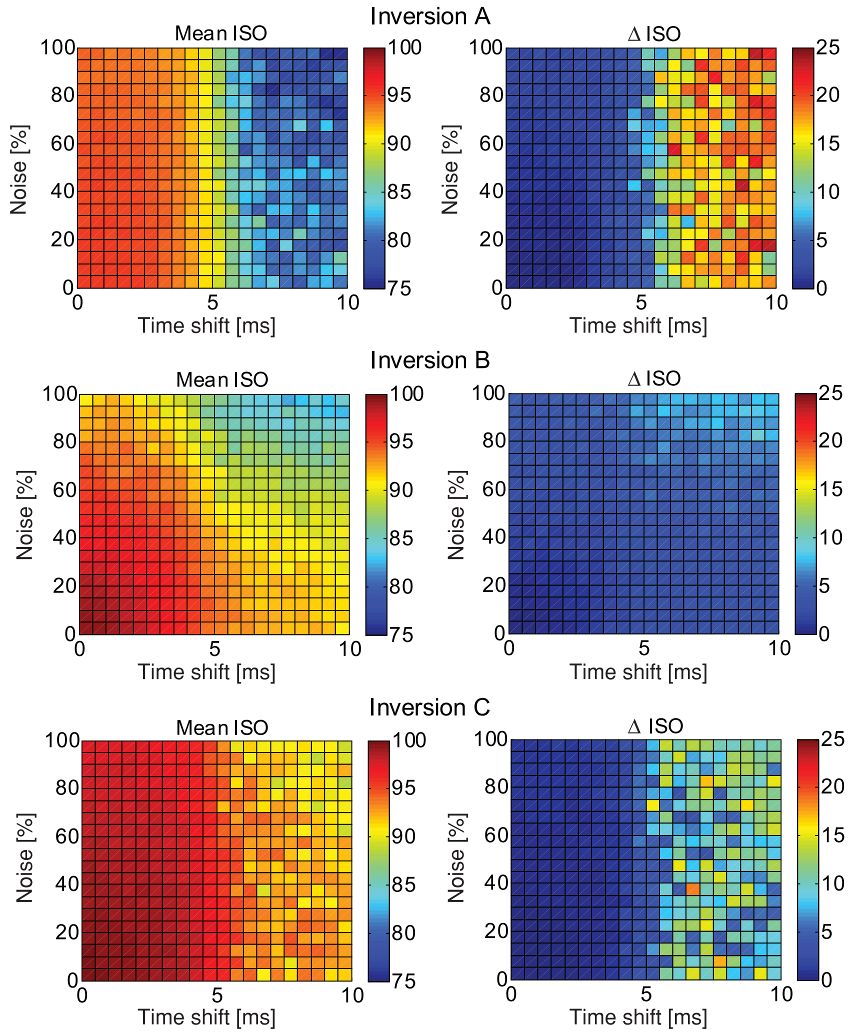

Figure 8. Inversion for the explosive source: ISO percentage. Mean values (left-hand side plots) and standard deviations (right-hand side plots) of the ISO percentages are shown for Inversion A (upper plots), Inversion B (middle plots) and Inversion C (lower plots) as a function of noise in time shifts (x-axis) and in amplitudes (y-axis). The colour-coded mean values and standard deviations are in per cent.

Table 3. Inversion of the pure explosive source.

	abs(ISO) (per cent)	abs(CLVD) (per cent)	DC (per cent)
True values	100.0	0.0	0.0
Noise-free data			
Inversion A	95.4	2.5	2.1
Inversion B	99.4	0.2	0.4
Inversion C	99.9	0.0	0.1
Noisy data			
Inversion A	91.3	3.5	5.2
Inversion B	91.9	2.9	5.2
Inversion C	96.5	1.5	2.0

Noisy data: maximum amplitude noise is 50 per cent, maximum noise in time shifts is 5 ms, mean values over 100 realizations of random noise are presented. Quantities abs(ISO) and abs(CLVD) are absolute values of ISO and CLVD, respectively.

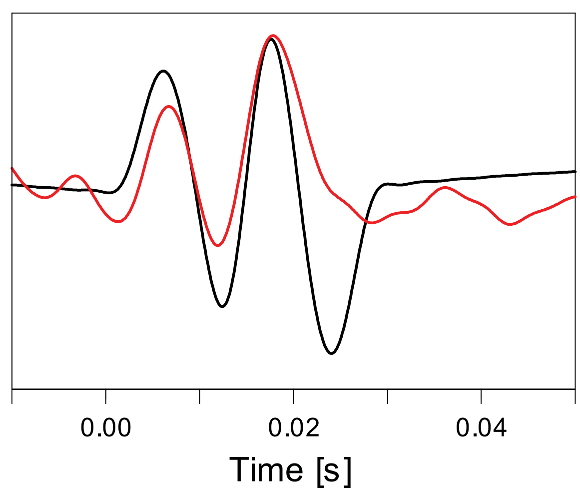

Figure 9. Second derivative of the source-time function retrieved from noise-free (black) and noisy (red) waveforms of the explosive source. The inverted noisy waveforms are contaminated with noise in amplitudes up to 25 per cent and with noise in arrival times up to 5 ms.

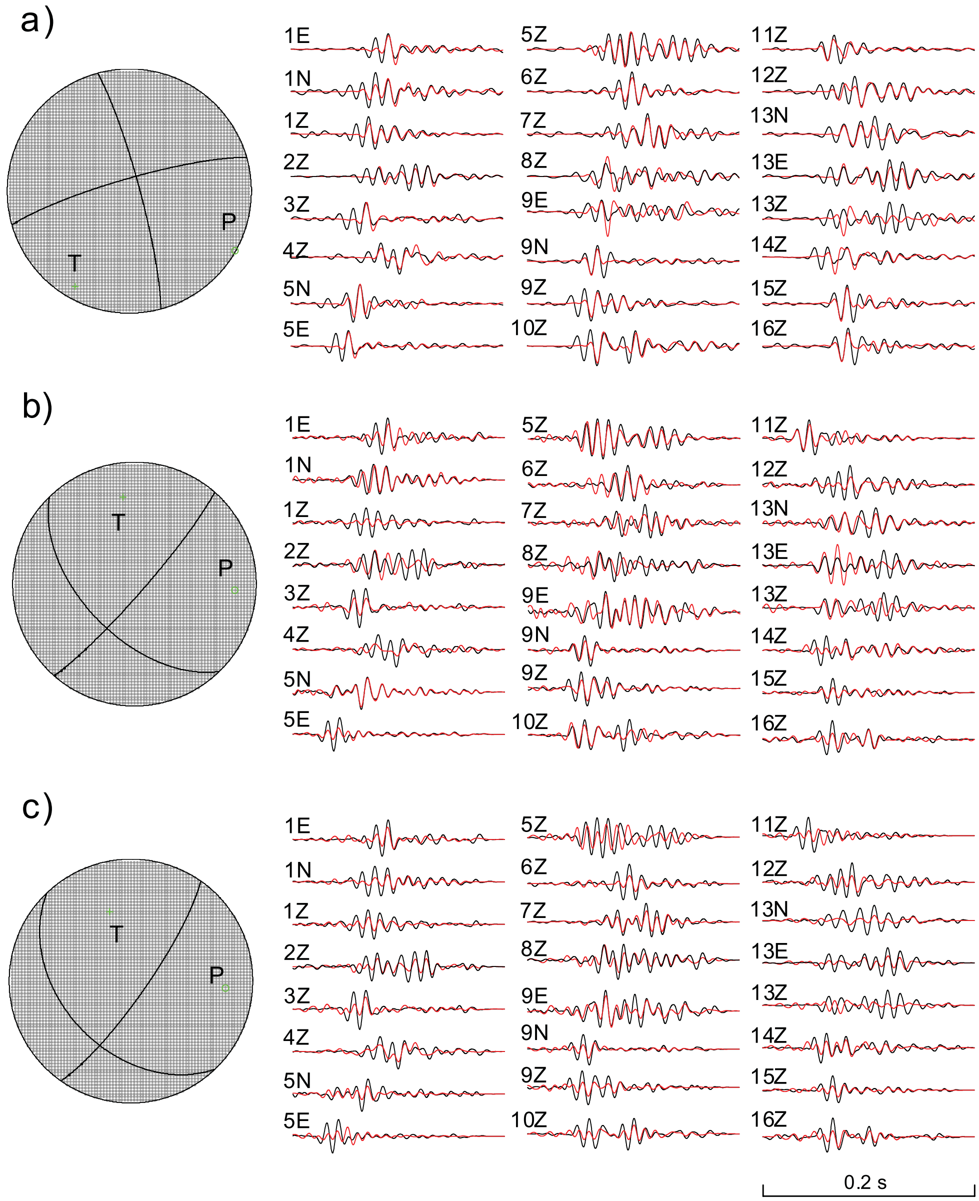

Figure 10. Inversion for the explosive source: the focal mechanisms and the fit between the synthetic and observed data for Inversion A (upper plots), Inversion B (middle plots) and Inversion C (lower plots). Red lines—synthetic waveforms, black lines—observed data. The inverted waveforms are contaminated with noise in amplitudes up to 25 per cent and with noise in arrival times up to 5 ms.

longer than 200 m, large parts of energy are transferred into a *P*- and *S*-wave coda produced by scattering because of strong velocity contrasts between different rock types, the excavation area and the tunnel system (see Oye *et al.* 2005).

The velocity model is strongly inhomogeneous because of the presence of large excavation volumes with complex geometries. The mining infrastructure, including excavation volumes, tunnels, stopes and passes, is repeatedly measured by laser scanning and a model is built using mine design software. Fig. 11(b) shows a detailed 3-D velocity model available on a 2-m grid, which was recorded in 2003. The ore body is displayed in brown, the mined-out cavities in green (the host rock is not depicted) and pink dots mark geophone positions. Table 1 describes the seismic properties of the model.

4.2 Data

Observations of a production blast fired on 2003 January 14 at 21:59:24.4 and of a rockburst that occurred on 2003 August 27 at 20:15:59.9 have been processed. We analysed 24 and 21 records with a good signal-to-noise ratio for the blast and for the rockburst, respectively. The records were resampled to a uniform sampling rate of 10 kHz. Because the velocity model is strongly heterogeneous, the blast and the rockburst were located using a full grid search of traveltime tables computed with the eikonal solver (Podvin & Lecomte 1991). This method provides accurate first arrival *P*- and *S*-wave onset times even in very heterogeneous media where ray tracing may fail (Gharti *et al.* 2008). The principle of reciprocity was employed for computation of the traveltime tables: receiver

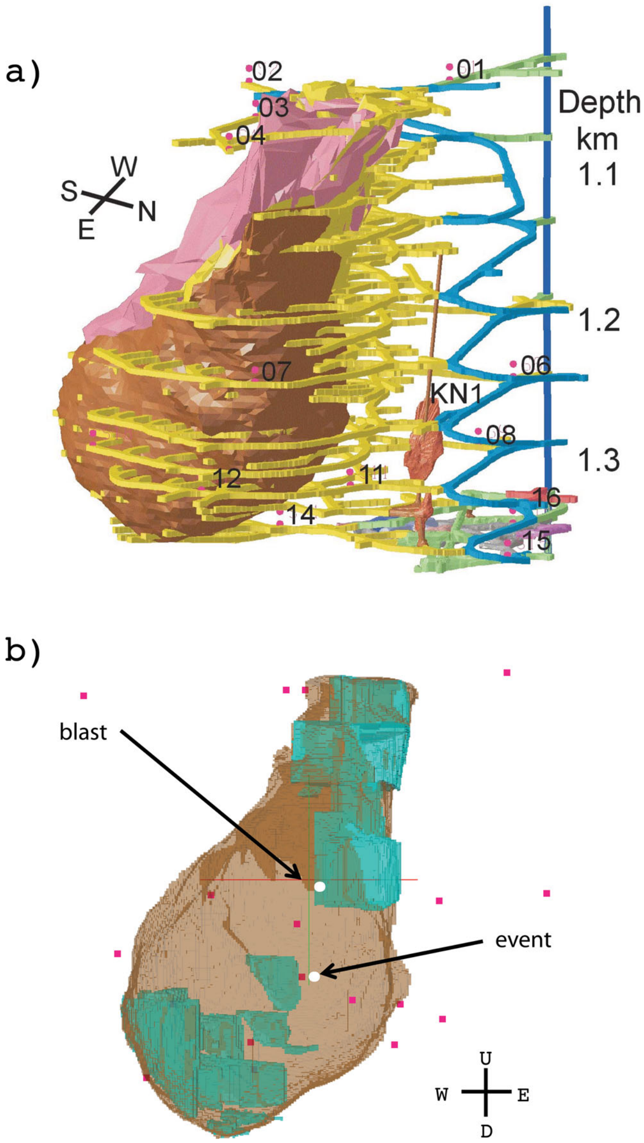

Figure 11. The complex system of corridors and tunnels in the Pyhäsalmi ore mine, Finland (a) and positions of seismic sensors in the mine (b). The ore body is in brown and in magenta in plot (a), and in light and dark brown in plot (b). The excavation area is marked in green colour (b). The red dots in (b) mark the seismic sensors.

positions were considered as source locations and the traveltimes were stored at all grid points, serving as potential source positions during event location. The obtained locations are shown in Fig. 11(b). The distances from the sources to the stations are between 55 and 370 m.

The Green's functions were computed using the 3-D finite difference viscoelastic code E3D (Larsen & Grieger 1998) as implemented by Gharti *et al.* (2008). The spatial sampling is 2 m, the sampling frequency is 10 kHz. The central frequency of the Gaussian source pulse is 350 Hz. Data as well as Green's functions are filtered by a two-sided Butterworth high-pass filter with a corner frequency of 30 Hz to remove low-frequency noise.

4.3 Results of the moment tensor inversion

Similarly as in the modelling section, the inversion was stabilized by applying low-pass filtering to data and Green's functions. The corner frequencies were: 100 Hz (both for Green's functions and data) in Inversion A, and 250Hz (for Green's functions) and 120 Hz (for data) in Inversions B and C. Subsequently, three inversion methods were applied: simple time-domain inversion (Inversion A), frequency-domain inversion (Inversion B), and the two-step time-frequency inversion (Inversion C).

For the blast, all three inversions produce positive ISO components with values higher than 65 per cent indicating that the inversion was successful (see Figs 12 and 13; Table 4). The CLVD percentage is minor but also positive. The largest DC and the lowest ISO percentages are predicted by Inversion A. As expected, the best fit between data and synthetics is produced by Inversion B because this method minimizes the misfit using more parameters. However, the most reliable value of the ISO percentage is probably obtained using Inversion C. The orientation of the DC part is consistent for all three solutions (see Table 4). This may indicate that the DC part is not only an error of the inversion.

The stability and robustness of the results is tested similarly as for the synthetic data by repeated inversions of data contaminated by random noise. The level of noise varies from 0 (noise-free data) to 50 per cent in steps of 5 per cent. The maximum random time shift varies from 0 to 5 ms in steps of 0.5 ms. To get statistically relevant results, we have inverted data for 100 realizations of random noise for each noise level. Because all combinations of 10 levels of amplitude noise and 10 levels of random time shift were calculated, the figures summarize the results of 10.000 inversions.

Fig. 14 shows that the ISO percentage is quite stable ranging from 65 to 73 per cent for all three inversion methods and for all levels of noise. The figures indicate a slight tendency of increasing the ISO percentage with increasing noise. This resembles the results of synthetic modelling of the inversion of the DC source (Fig. 5), when noisy data displayed spurious ISO components. Therefore, we conclude that the ISO increase in Fig. 14 may also be spurious and the true ISO percentage is probably not higher than 68–70 per cent. This indicates that the source mechanism of the blast is not simple and may contain non-isotropic components produced by minor shearing triggered by the blast or by material inhomogeneities or anisotropy near the source.

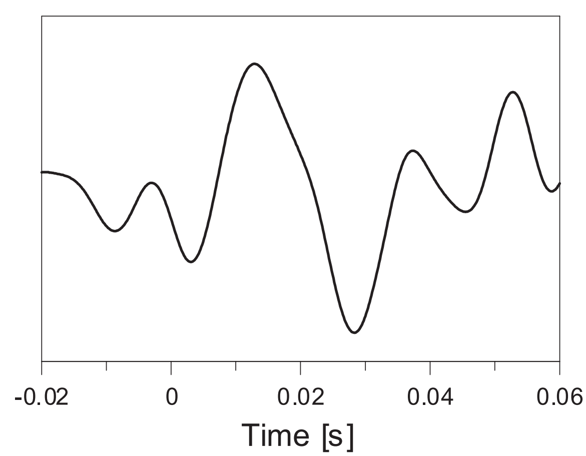

Figure 12. Second derivative of the source-time function retrieved for the production blast.

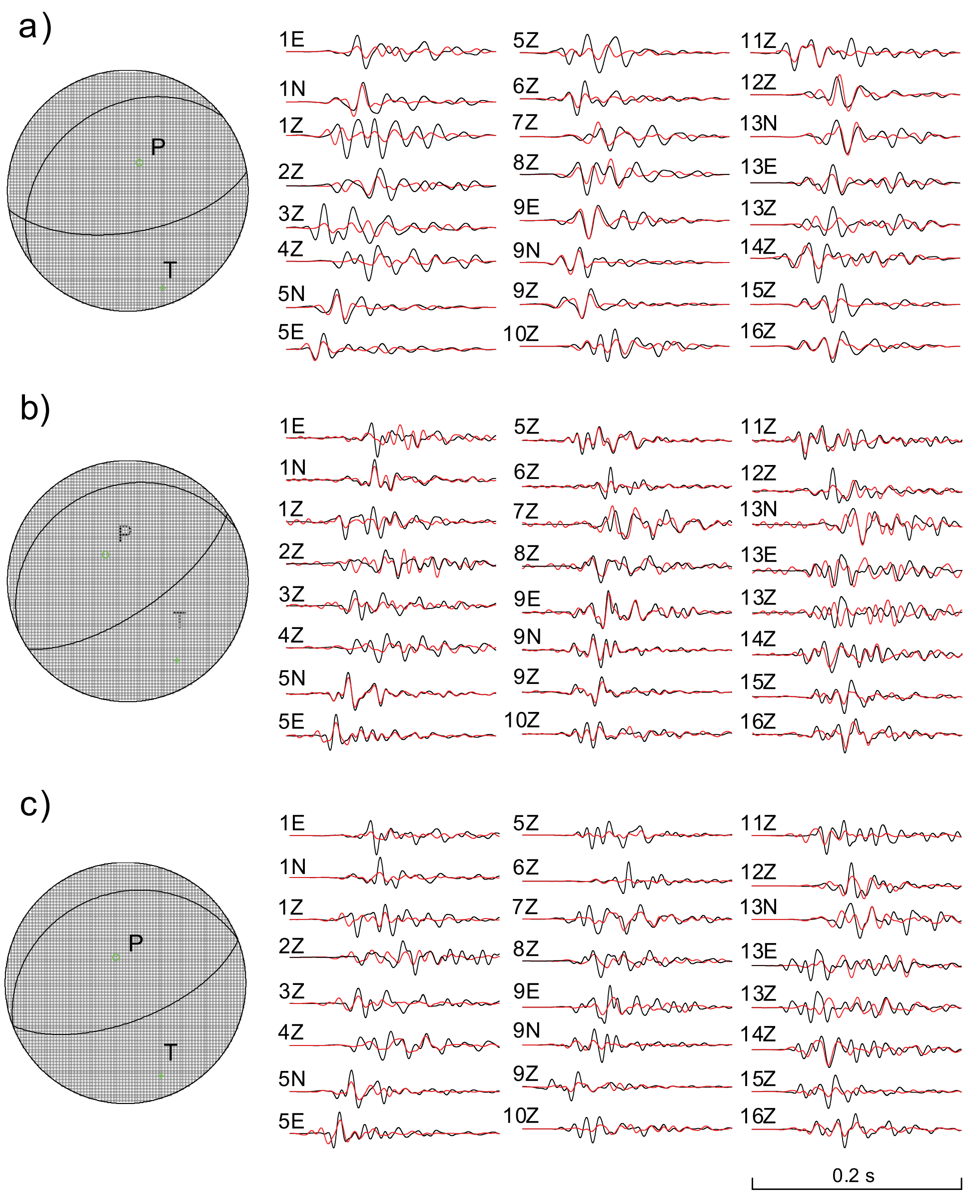

Figure 13. Inversion for the blast: the focal mechanisms (left-hand side plots) and the fit between the synthetic (red line) and observed (black line) data (right-hand side plots) for Inversion A (upper plots), Inversion B (middle plots) and Inversion C (lower plots).

Table 4. Inversion of real observations.

Method	ISO (per cent)	CLVD (per cent)	DC (per cent)	Strike (°)	Dip (°)	Rake (°)
Blast						
Method A	66	15	19	81	62	−75
Method B	71	27	2	56	68	−93
Method C	68	26	6	69	64	−90
Rockburst						
Method A	−62	−1	37	88	36	134
Method B	−67	−12	21	85	53	145
Method C	−69	−5	26	94	48	145

For the rockburst, the three inversions also produce consistent results (see Figs 15 and 16). The ISO components are less than −60 per cent (see Table 4). The CLVD percentage is minor, but also negative. The orientation of the DC part is similar for all three solutions (see Fig. 16; Table 4). This indicates that the DC part may partly reflect the presence of minor shear mechanism in a predominantly implosive source. The stability of the results is tested in the same way as for the blast (see Fig. 17). The tests indicate that the results are mostly sensitive to errors in time (produced by mislocation and/or velocity mismodelling). Similar to the numerical modelling, Inversion B displays a tendency of increasing the absolute value of the ISO percentage with increasing noise. On the contrary, Inversions A and C show an opposite tendency. The plots of the standard deviation of the ISO percentage of the blast and the rockburst (Fig. 17, right-hand side plots) indicate that for an error in time shifts higher than 2 ms, the ISO percentage becomes unreliable.

5 DISCUSSION AND CONCLUSIONS

The waveform inversions can produce moment tensors of diverse accuracy. The simple time-domain inversion, which neglects

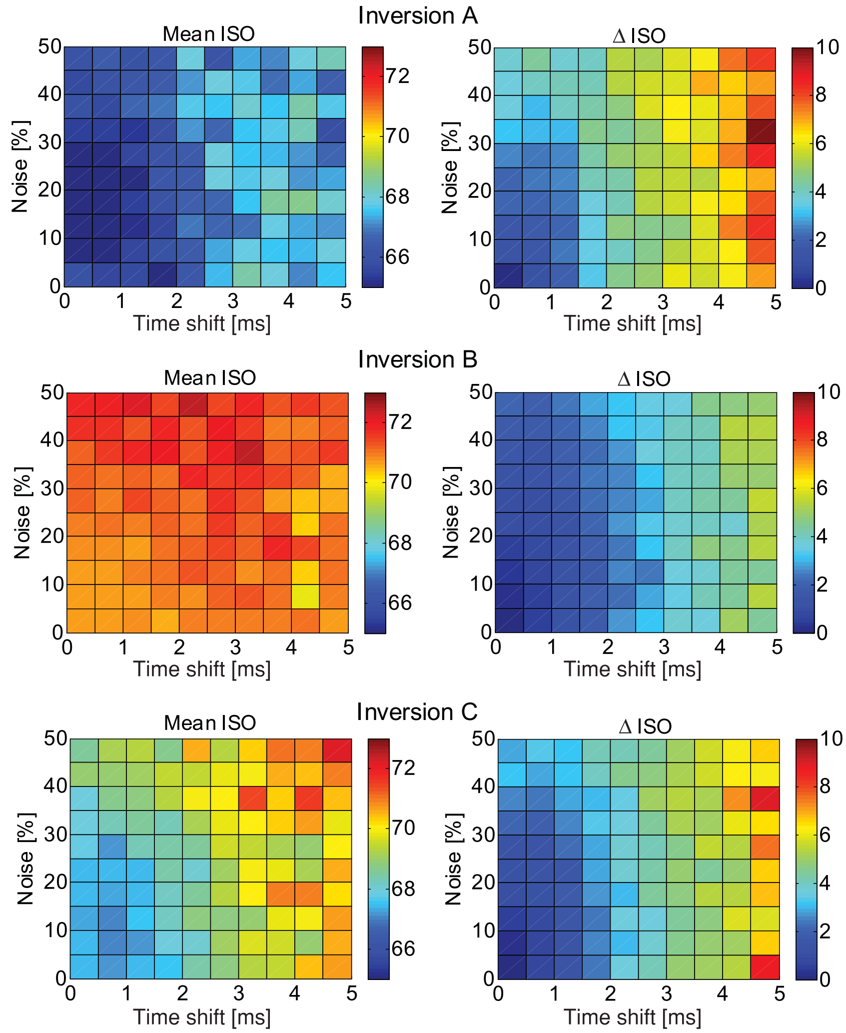

Figure 14. Inversion for the blast: ISO percentage. Mean values (left-hand side plots) and the standard deviations (right-hand side plots) of the ISO percentages are shown for Inversion A (upper plots), Inversion B (middle plots) and Inversion C (lower plots) as a function of noise in time shifts (x-axis) and of amplitude noise (y-axis). The colour-coded mean values and standard deviations are in per cent.

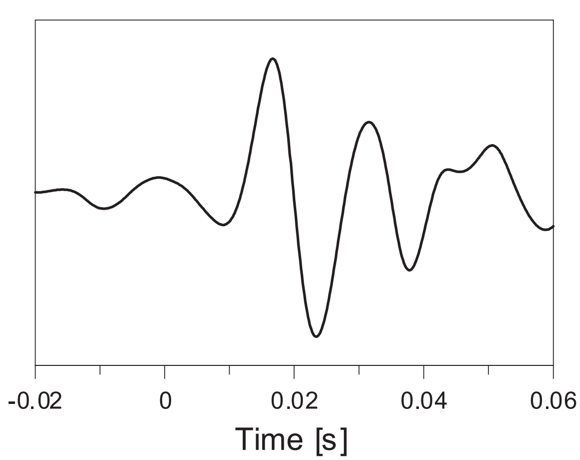

Figure 15. Second derivative of the source-time function retrieved for the rockburst.

complexities in the source-time function, is a robust method being rather insensitive to noise in the data and to inaccuracies in the event location and in the velocity model. However, the inversion requires heavy filtering of high frequencies and produces biased results for sources with a complex source-time history. On the other hand, the frequency-domain waveform inversion based on complex spectra operates in a broader frequency range than the time-domain inversion and may retrieve in addition a source-time function. The method produces accurate and unbiased moment tensors for noise-free data, but its accuracy remarkably decreases and results in a very high spurious ISO component if the data are noisy, and the event location or the velocity model are inaccurate. Therefore, this method is preferable for high-quality data with accurate event locations and good knowledge of the model. The advantages of both inversion methods are retained in the proposed two-step time-frequency method. This method yields accurate and unbiased moment tensors for high-quality data of sources with a complex source-time history. Moreover, the method yields accurate moment tensors even for low-quality data, being rather insensitive to inaccuracies in the location and in the velocity model.

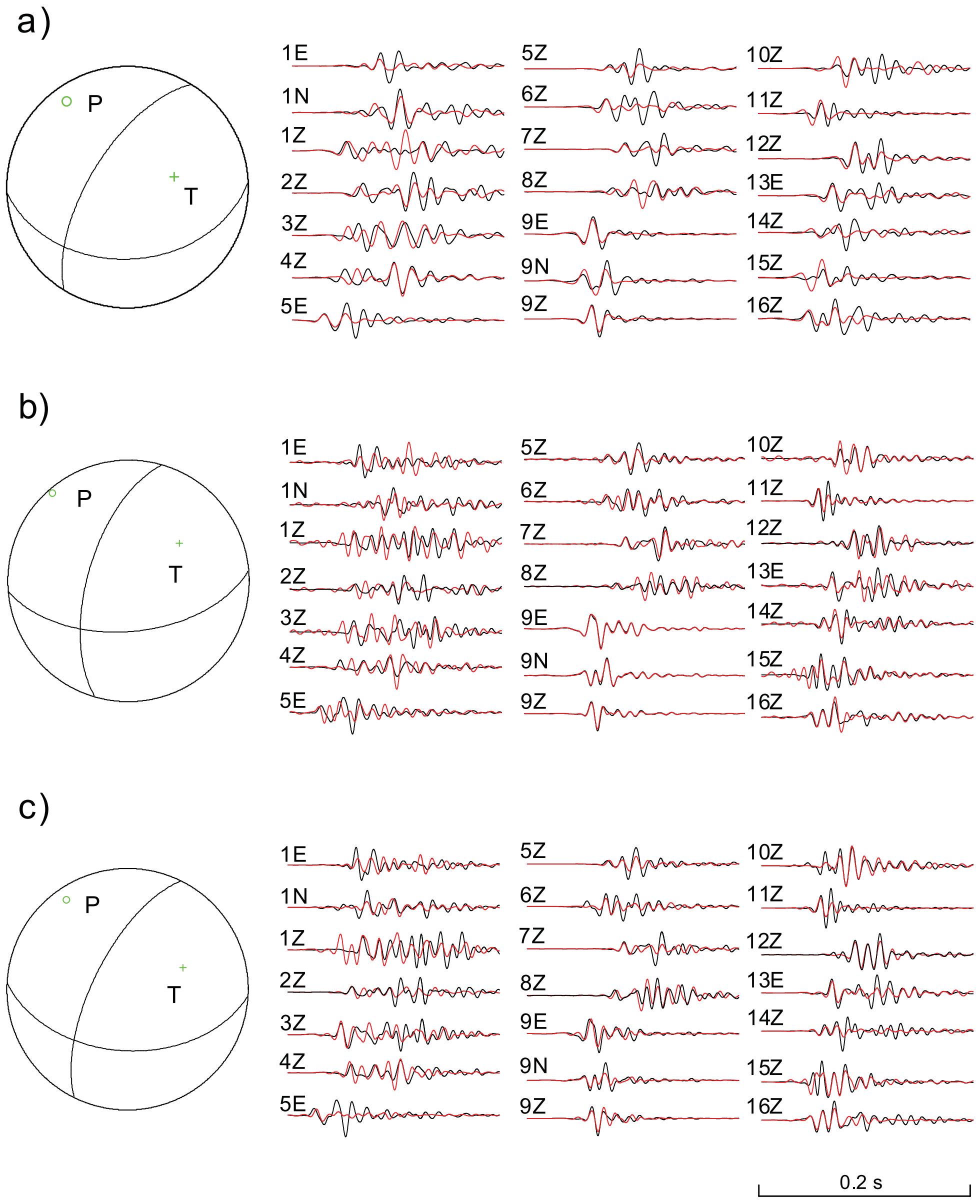

Figure 16. Inversion for the rockburst: the focal mechanisms (left-hand side plots) and the fit between the synthetic (red line) and observed (black line) data (right-hand side plots) for Inversion A (upper plots), Inversion B (middle plots) and Inversion C (lower plots).

The results of the proposed moment tensor inversion applied to observations of a blast and a rockburst in the Pyhäsalmi ore mine indicate that the inversion was successful even in a complex geological environment with large excavation volumes. The ISO component is high and positive for the production blast, and high but negative for the rockburst. The DC component is minor but consistent for all tested inversion methods. Similar to the numerical modelling, the application to real data indicates that the two-step time-frequency approach is robust and produces the most reliable moment tensors compared to the other two inversion schemes.

The repeated inversions of synthetic as well as observed data contaminated by artificial random noise in amplitudes and time shifts of waveforms proved to be a useful tool for assessing the stability and robustness of the moment tensor inversion methods. The stability tests are important, particularly, in analysis of observations providing us with information about the sensitivity of the results to mislocation and mismodelling and, consequently, about the accuracy of the focal mechanisms as well as the DC and non-DC percentages.

ACKNOWLEDGMENTS

We thank Frank Krüger, Jiří Zahradník and one anonymous reviewer for their reviews, Volker Oye and Michael Roth for fruitful discussions, Hom Nath Gharti for help with calculations of the Green's functions in the Pyhäsalmi ore mine, Katja Sahala (INMET Mining Co.) and the ISS International Ltd for access to the mine model and the in-mine data. Further, we thank Shawn Larsen for his E3D code, and Pascal Podvin for his eikonal solver. The work was supported by the Grant Agency of the Academy of Sciences of the Czech Republic, Grant No. IAA300120801, by the Grant Agency of the Czech Republic, Grant No. P210/12/1491, by the European Community's FP7 Consortium Project AIM 'Advanced Industrial Microseismic Monitoring', Grant Agreement

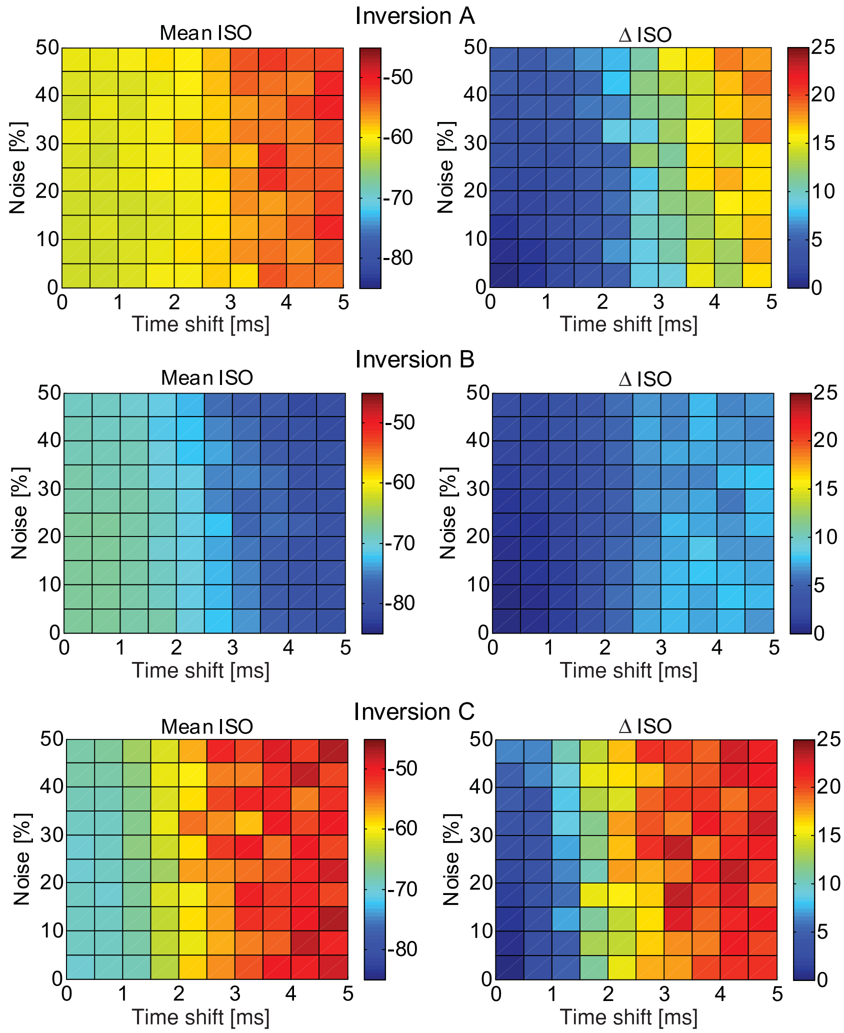

Figure 17. Inversion for the rockburst: ISO percentage. Mean values (left-hand side plots) and the standard deviations (right-hand side plots) of the ISO percentages are shown for Inversion A (upper plots), Inversion B (middle plots) and Inversion C (lower plots) as a function of noise in time shifts (x-axis) and of amplitude noise (y-axis). The colour-coded mean values and standard deviations are in per cent.

No. 230669 and by the SAFECO2 Project funded by the Norwegian Research Foundation, Grant No. 189994.

REFERENCES

Adamová, P., Sokos, E. & Zahradník, J., 2009. Problematic non-double-couple mechanism of the 2002 Amfilochia Mw5 earthquake, Western Greece, *J. Seism.,* **13,** 1–12.

Aki, K. & Richards, P.G., 2002. *Quantitative Seismology,* University Science Books, Sausalito, CA.

Cesca, S., Buforn, E. & Dahm, T., 2006. Amplitude spectra moment tensor inversion of shallow earthquakes in Spain, *Geophys. J. Int.,* **166,** 839–854.

Cesca, S. & Dahm, T., 2008. A frequency domain inversion code to retrieve time-dependent parameters of very long period volcanic sources, *Comput. Geosci.,* **34,** 235–246.

Cesca, S., Heimann, S., Stammler, K. & Dahm, T., 2010. Automated procedure for point and kinematic source inversion at regional distances, *J. geophys. Res.,* **115,** B06304, doi:10.1029/2009JB006450.

Dreger, D. & Woods, B., 2002. Regional distance seismic moment tensors of nuclear explosions, *Tectonophysics,* **356,** 139–156.

Dziewonski, A.M., Chou, T.A. & Woodhouse, J.H., 1981. Determination of earthquake source parameters from waveform data for studies of regional and global seismicity, *J. geophys. Res.,* **86,** 2825–2852.

Gharti, H.N., Oye, V. & Roth, M., 2008. Travel times and waveforms of microseismic data in heterogeneous media, *SEG Expanded Abstr.,* **27,** 1337–1341, doi:10.1190/1.3059162.

Godano, M., Bardainne, T., Regnier, M. & Deschamps, A., 2011. Moment-tensor determination by nonlinear inversion of amplitudes, *Bull. seism. Soc. Am.,* **101,** 366–378.

Hardebeck, J.L. & Shearer, P.M., 2003. Using S/P amplitude ratios to constrain the focal mechanisms of small earthquakes, *Bull. seism. Soc. Am.,* **93,** 2432–2444.

Hingee, M., Tkalčić, H., Fichtner, A. & Sambridge, M., 2011. Seismic moment tensor inversion using a 3-D structural model: applications for the Australian region, *Geophys. J. Int.,* **184,** 949–964.

Fojtíková, L., Vavryčuk, V., Cipciar, A. & Madarás, J., 2010. Focal mechanisms of micro-earthquakes in the Dobrá Voda seismoactive area in the Malé Karpaty Mts. (Little Carpathians), Slovakia, *Tectonophysics,* **492,** 213–229, doi:10.1016/j.tecto.2010.06.007.

Jechumtálová, Z. & Šílený, J., 2001. Point-source parameters from noisy waveforms: error estimate by Monte-Carlo simulation, *Pure appl. Geophys.,* **158,** 1639–1654.

Jechumtálová, Z. & Šílený, J., 2005. Amplitude ratios for complete moment tensor retrieval, *Geophys. Res. Lett.,* **32,** L22303, doi:10.1029/2005GL023967.

Jolliffe, I.T., 1986. *Principal Component Analysis,* Springer Verlag, New York, NY.

Kikuchi, M. & Kanamori, H., 1991. Inversion of complex body waves—III, *Bull. seism. Soc. Am.,* **81,** 2335–2350.

Larsen, S. & Grieger, J., 1998. Elastic modeling initiative: Part 3—3-D computational modeling. *SEG Expanded Abstr.,* **17,** 1803–1806.

Menke, W., 1989. *Geophysical Data Analysis: Discrete Inverse Theory,* Int. geophys. Ser. Vol. 45, Academic Press, New York, NY.

Miller, A.D., Julian, B.R. & Foulger, G.R., 1998. Three-dimensional seismic structure and moment tensors of non-double-couple earthquakes at the Hengill-Grensdalur volcanic complex, Iceland, *Geophys. J. Int.,* **133,** 309–325.

Oye, V., Bungum, H. & Roth, M., 2005. Source parameters and scaling relations for mining-related seismicity within the Pyhäsalmi ore mine, Finland, *Bull. seism. Soc. Am.,* **95,** 1011–1026, doi:10.1785/0120040170.

Podvin, P. & Lecomte, I., 1991. Finite difference computation of traveltimes in very contrasted velocity models: a massively parallel approach and its associated tools, *Geophys. J. Int.,* **105,** 271–284.

Puustjärvi, H., 1999. Pyhäsalmi Modeling Project, Section B. Geology, Technical Report, Geological Survey of Finland and Outokumpu Mining Oy, 66pp.

Sokos, E. & Zahradník, J., 2008. ISOLA—a Fortran code and Matlab GUI to perform multiple point source inversion of seismic data, *Comput. Geosci.,* **34,** 967–977.

Šílený, J., 1998. Earthquake source parameters and their confidence regions by a genetic algorithm with a 'memory', *Geophys. J. Int.,* **134,** 228–242.

Šílený, J., Panza, G.F. & Campus, P., 1992. Waveform inversion for point source moment tensor retrieval with variable hypocentral depth and structural model, *Geophys. J. Int.,* **109,** 259– 274.

Sipkin, S.A., 1986. Estimation of earthquake source parameters by the inversion of waveform data: Global seismicity, 1981–1983, *Bull. seism. Soc. Am.,* **76,** 1515–1541.

Vallée, M., Charléety, J., Ferreira, A.M.G., Delouis, B. & Vergoz, J., 2011. SCARDEC: a new technique for the rapid determination of seismic moment magnitude, focal mechanism and source time functions for large earthquakes using body-wave deconvolution, *Geophys. J. Int.,* **184,** 338–358.

Vasco, D.W., 1989. Deriving source-time functions using principal component analysis, *Bull. seism. Soc. Am.,* **79,** 711–730.

Vavryčuk, V., 2001. Inversion for parameters of tensile earthquakes, *J. geophys. Res.,* **106**(B8), 16.339–16.355, doi:10.1029/2001JB000372.

Vavryčuk, V., 2004. Inversion for anisotropy from non-double-couple components of moment tensors, *J. geophys. Res.,* **109,** B07306, doi:10.1029/2003JB002926.

Vavryčuk, V., 2011a. Principal earthquakes: theory and observations for the 2008 West Bohemia swarm, *Earth planet. Sci. Lett.,* **305,** 290–296, doi:10.1016/j.epsl.2011.03.002.

Vavryčuk, V., 2011b. Detection of high-frequency tensile vibrations of a fault during shear rupturing: observations from the 2008 West Bohemia swarm, *Geophys. J. Int.,* **186,** 1404–1414., doi:10.1111/j.1365-246X.2011.05122.x.

Vavryčuk, V., 2011c. Tensile earthquakes: theory, modeling, and inversion, *J. geophys. Res.,* **116,** B12320, doi:10.1029/2011JB008770.

Vavryčuk, V., Bohnhoff, M., Jechumtálová, Z., Kolář, P. & Šílený, J., 2008. Non-double-couple mechanisms of micro-earthquakes induced during the 2000 injection experiment at the KTB site, Germany: a result of tensile faulting or anisotropy of a rock?, *Tectonophysics,* **456,** 74–93, doi:10.1016/j.tecto.2007.08.019.

Wéber, Z., 2009. Estimating source time function and moment tensor from moment tensor rate functions by constrained L1 norm minimization, *Geophys. J. Int.,* **178,** 889–900.

Zahradník, J., Serpetsidaki, A., Sokos, E. & Tselentis, G-A., 2005. Iterative deconvolution of regional waveforms and double-event interpretation of the 2003 Lefkada earthquake, Greece, *Bull. seism. Soc. Am.,* **95,** 159–172.

Zahradník, J., Janský, J. & Plicka, V., 2008a. Detailed waveform inversion for moment tensors of M 4 events: examples from the Corinth Gulf, Greece, *Bull. seism. Soc. Am.,* **98,** 2756–2771.

Zahradník, J., Sokos, E., Tselentis, G.-A. & Martakis, N., 2008b. Nondoublecouple mechanism of moderate earthquakes near Zakynthos, Greece, April 2006; explanation in terms of complexity, *Geophys. Prospect.,* **56,** 341–356.